$Yb_2Si_2O_7$ Environmental Barrier Coatings Deposited by Various Thermal Spray Techniques: A Preliminary Comparative Study

Emine Bakan*, Diana Marcano, Dapeng Zhou, Yoo Jung Sohn, Georg Mauer, Robert Vaßen

Forschungszentrum Jülich GmbH, Institute of Energy and Climate Research IEK-1, 52425 Jülich, Germany

*Corresponding Author. Forschungszentrum Jülich GmbH, Institute of Energy and Climate Research IEK-1, 52425 Jülich, Germany. Tel: +49 2461 61 2785; Fax: +49 2461 61 2455, e-mail: e.bakan@fz-juelich.de.

Abstract

Dense, crack-free, uniform and well-adhered environmental barrier coatings (EBCs) are required to enhance the environmental durability of silicon (Si)-based ceramic matrix composites (CMCs) in high pressure, high gas velocity combustion atmospheres. This paper represents an assessment of different thermal spray techniques for the deposition of $Yb_2Si_2O_7$ EBCs. The $Yb_2Si_2O_7$ coatings were deposited by means of atmospheric plasma spraying (APS), high-velocity oxygen fuel spraying (HVOF), suspension plasma spraying (SPS), and very low-pressure plasma spraying (VLPPS), techniques. The initial feedstock, as well as the deposited coatings, were characterized and compared in terms of their phase composition. The as-sprayed amorphous content, microstructure, and porosity of the coatings were further analyzed. Based on this preliminary investigation, the HVOF process stood out from the other techniques as it enabled the production of vertical crack-free coatings with higher crystallinity in comparison with the APS and SPS techniques in atmospheric conditions. Nevertheless, VLPPS was found to be the preferred process for the deposition of $Yb_2Si_2O_7$ coatings with desired characteristics in a controlled atmosphere chamber.

Keywords: environmental barrier coating (EBC), ceramic matrix composite (CMC), thermal spray, ytterbium silicate

1. Introduction

An improvement in the temperature capability of high-strength materials is crucial for developments in advanced gas turbine technology. As current film-cooled and thermal barrier coating protected single-crystal superalloy components have already reached their limit in terms of performance, ceramic matrix composites (CMCs) are regarded as the new material of choice for such components. SiC/SiC CMCs, for example, offer higher temperature capability (about 400°C higher compared to the best superalloy), good mechanical strength, thermal shock resistance, and, moreover, they are lightweight. These characteristics can be used to reduce the weight of aircraft, while higher turbine inlet temperatures are reached with less cooling air, which in turn result in greater efficiency.

One main obstacle to substituting Si-based ceramics for metallic components is their degradation when exposed to water vapor-rich fast-flowing gasses in high-temperature and pressure combustion environments [1-5]. Furthermore, the CMCs suffer from severe hot corrosion in molten salt [6]. Environmental barrier coatings (EBCs) [7] are therefore needed for the protection of Si-based CMCs in order to increase their durability in combustion environments. Beginning in the late 1990s, research and development at NASA introduced multilayer EBC systems, which were subsequently successfully tested in gas turbine engines [7-9]. In these EBC systems, silicon bond coats were applied for the oxidation protection of the substrate as well as to improve the adhesion of the coatings on it. Different top coat layers with high water vapor stability were deposited on the silicon bond coats to impede the diffusion of oxygen and water vapor through the substrate. Mullite and barium-strontium-aluminosilicate (BSAS) were used for this purpose in the early generation EBCs [10]. Lee et al. [11] later on experimentally compared the environmental stability of BSAS and two types of RE silicates: mono- and disilicates (RE_2O_3–SiO_2 and RE_2O_3–$2SiO_2$) in combustion environments and observed that the RE monosilicates have a higher stability in water vapor than BSAS and RE disilicates. Furthermore, the superior chemical stability of some RE silicates (Yb, Lu, Sc silicates) compared to the BSAS was reported in this study and, consequently, later generation EBCs consisting of RE silicate top coats were established. In the

meantime, the deposition of mullite and RE silicates by APS was investigated and found to be quite challenging due to the high glass-forming tendency of silicates and the high solidification rates in the process; as-sprayed coatings were reported to be highly amorphous [12]. These issues are also familiar from the plasma spraying of YAG and hexaaluminate coatings [13-15]. The amorphous deposits are not desired as crystallization induced shrinkage at elevated temperatures leads to crack formation and spallation of the coatings. To avoid that, NASA suggested a modification in the plasma spray process in which particles are sprayed on a substrate placed in a furnace and heated up to 1000°C [16]. Increasing the substrate temperature above the glass transformation temperature of the sprayed material ensures the nucleation and growth of the crystal nuclei, which results in highly crystalline silicate coatings being produced by this method [11] [17-19]. Over the last two decades, EBC systems (e.g. bilayer, trilayer, multilayer) featuring different RE silicates were also manufactured using alternative processing techniques by different groups (**Table 1**). However, the same amorphous deposit problem was addressed for each deposition method in which the melting\vaporization of the coating material and the subsequent rapid solidification of it on the substrate take place. ~~After heat treatments, undesirable, shrinkage-induced crack formations were observed in these coatings.~~ When using wet chemical deposition methods, however, highly crystalline coatings were deposited. Nonetheless, a gaseous bubble formation was observed at the coating–substrate interface using the dip-coating technique, which likely has an adverse effect on the adhesion of the coatings. A sol–gel method involving high-temperature (1550°C) sintering for densification of the layer does not seem to be applicable to a system that includes a Si bond layer, as it would exceed the melting temperature of Si (1400°C). Ultimately, modified plasma spraying seems to be the only well-functioning technique among the other reported studies. However, the feasibility of transferring such spraying technology to real components with complicated shapes remains an important question.

Another processing issue of silicate EBCs is the deposition of stoichiometric coatings, which are dense at the same time [20]. Associated with the preferential volatilization of Si-bearing species from the molten

particles during the spraying process, Si-depleted coatings were obtained when compared to starting powders. In particular, high-power processing to ensure dense silicate coatings was found to be conducive to the formation of stoichiometric coatings, since higher heat transfer from plasma to particles further boosts the evaporation of species with high vapor pressure [21]. Similar processing issues and the resulting detrimental effects of secondary phases present in the as-sprayed coatings of different groups of materials (e.g. pyrochlores, perovskites) are often reported in the literature [22-25].

From a materials' perspective, Yb_2SiO_5 (YbMS) and $Yb_2Si_2O_7$ (YbDS) are the most extensively studied group of EBCs to date, as can be seen in **Table 1**. Although the investigation of Lee et al. [11] favors the potential of RE monosilicates with high stability against water, the comparison of YbMS and YbDS reveals a substantially higher coefficient of thermal expansion (CTE) of the former ($7.4 \times 10^{-6}\,K^{-1}$ [17]) than that of the latter ($4.1 \times 10^{-6}\,K^{-1}$ [20]) as well as of SiC ($4.7 \times 10^{-6}\,K^{-1}$). The significant CTE mismatch between YbMS and SiC is therefore said to result in the formation of unfavorable cracks, which provide diffusion paths to the oxygen and water vapor through the YbMS coatings [20].

Taking these findings into account, we investigated the YbDS coatings deposited by various thermal spray deposition techniques. This paper provides a comparison of the microstructure, crystallinity, and phase composition of YbDS coatings deposited by means of APS, high-velocity oxygen-fuel (HVOF), suspension plasma spray (SPS), and very low-pressure plasma spraying (VLPPS).

2. Experimental

2.1 Powder feedstock and suspension

$Yb_2Si_2O_7$ powder provided by Oerlikon Metco (US) Inc. (Westbury, New York, USA) was used in this study for the deposition of coatings by APS. Part of this powder was sieved and the particle fractions captured on and under the sieve were used for the VLPPS and HVOF processes, respectively. Particle size distributions of the fractions measured by laser diffraction (LA-950-V2, Horiba Ltd., Japan) and dynamic light scattering (LB-550, Horiba Ltd., Japan) are shown in **Table 2**. For the SPS process, the $Yb_2Si_2O_7$

powder was synthesized from stoichiometric amounts of YbO_2 (99.9%, Treibacher Industrie AG, Austria) and SiO_2 (99.5%, VWR International GmbH, Germany). An ethanol-based suspension of this mixture was mechanically activated in a tumbling mixer (150 min^{-1}) with ZrO_2 milling balls for 24 hours. The obtained powder was dried and sintered at 1400˚C for 12 h. For SPS purposes, this powder was dispersed in ethanol with the addition of polyethylenimine (PEI) (Polysciences, Inc., Warrington, PA, USA) and ZrO_2 milling balls (d=3 mm, Sigmund Lindner GmbH, Warmensteinach, Germany). The mixture was milled on a roller bank (120 min^{-1}, 24 h). The particle size values after milling are given in **Table 2**. Finally, the obtained suspension was diluted with ethanol to a final solid content of 10 wt. %. The dynamic viscosity of the suspension was determined by the Physica MCR 301 rheometer from Anton Paar, with the viscosity measured to be 1.55 mPa.s at a shear rate of 10 s^{-1}. Samples of each raw material were investigated by means of scanning electronic microscopy (SEM) (Carl Zeiss NTS GmbH, Oberkochen, Germany) and X-ray diffraction (XRD) (D4 Endeavor, Bruker AXS GmbH, Karlsruhe, Germany) (Cu Kα radiation, operating voltage 40 kV, current 40 mA, step size 0.02 °, step time 0.75 s, 2θ range of 10–80°) for morphology and phase composition determination, respectively. XRD patterns of the micron-sized $Yb_2Si_2O_7$ powder (original powder, before sieving) with spherical particle morphology and submicron-sized $Yb_2Si_2O_7$ powder synthesized for the SPS process are shown in **Figure 1a-b**. Both XRD patterns yielded a crystalline structure with the presence of monoclinic $Yb_2Si_2O_7$ (*C*2/*m*, JCPDS No 01-082-0734) and secondary monoclinic Yb_2SiO_5 (*I*2/*a*, JCPDS No 00-040-0386) phases. Quantitative phase analysis (QPA) of the X-ray powder diffraction data was performed using the Rietveld analysis method (TOPAS software, Bruker Corporation, Germany) and micron- and submicron-sized powders were found to contain 5% and 39% Yb_2SiO_5, respectively.

2.2 Deposition of the coatings

Four different thermal spray systems were operated for the deposition of $Yb_2Si_2O_7$ coatings. A MultiCoat system (Oerlikon Metco, Wohlen, Switzerland) with three-cathode TriplexPro 210 and Diamond Jet 2700 spray torches mounted on a six-axis robot (IRB 2400, ABB, Switzerland) was employed for APS and

HVOF spray experiments, respectively. The HVOF burner was fitted with a convergent-cylindrical design nozzle (Type 2705) which yields lower particle velocities and thus longer dwell times in comparison to that of convergent-divergent nozzles [26]. A VLPPS investigation was performed with an O3CP torch operated by the MultiCoat platform (Oerlikon Metco, Wohlen, Switzerland) in a controlled-atmosphere chamber. Finally, an Axial III plasma torch with three separate cathode–anode pairs (Mettech Northwestern Corp., North Vancouver, BC, Canada) was used to generate the plasma jet for the SPS study and feedstock material was injected into the center of this plasma plume. A suspension-feeding system developed by Forschungszentrum Jülich GmbH (Germany) was used for spraying [27]. The spray parameters used for each experiment are listed in **Table 3**. High-power process conditions were selected for each spray method excluding the VLPPS technique to avoid vaporization but to obtain molten particles. Further information about the VLPPS method can be found here [28]. The temperature of the samples was monitored with a 4 M8 pyrometer (λ=13μm) (Land Instruments GmbH, Leverkusen, Germany) in the APS, HVOF, and SPS processes and an IR-AP pyrometer (λ=1.6μm) (Chino Corporation, Tokyo, Japan) in the VLPPS process. Square shape graphite (20x20x15mm) and carbon steel (25x25x2mm) served as substrate materials. All substrates were grit-blasted to an arithmetic average roughness (R_a) value range of 4.0-5.5μm and subsequently cleaned before spraying.

2.3 Characterization of deposited coatings

2.3.1 Amorphous content and quantitative phase analysis (QPA)

XRD measurements were performed on the as-deposited top coats with the same measurement parameters for the feedstock given above (D4 Endeavor & TOPAS software, Bruker AXS, Germany). The presence of amorphous content in the XRD patterns of as-sprayed coatings was detected and since QPA using the Rietveld method is limited to well-defined crystalline species, the PONKCS (partial or no known crystal structure) method was used for this purpose. The advantages of the PONKCS method for the QPA of the amorphous phases over the traditional Rietveld method or Reference Intensity Ratio (RIR) analysis are

reported here [29]. In the Rietveld method, the weight fraction of the *i*th crystalline phase in a mixture of *n* phases can be obtained from

$$W_i = \frac{S_i(ZMV)_i}{\sum_{j=1}^{n} S_j(ZMV)_j} \quad (1)$$

where S_i is the Rietveld scale factor for phase *i*, *ZM* is the mass of the unit cell contents, and *V* is the volume of the unit cell. The PONKCS method also follows this general form, but it includes the empirically derived $(ZMV)_a$ of the amorphous phase in Eq. (1). $(ZMV)_a$ can be determined by using a known mixture of the amorphous and crystalline sample for which the ZMV_c is known:

$$(ZMV)_a = \frac{W_a}{W_c}\frac{S_c}{S_a}(ZMV)_c \quad (2)$$

where W_a and W_c are the known weight fractions, S_a and S_c are the refined scale factors of the amorphous and crystalline samples, respectively. The background of the methodology is described in detail in [29]. For the derivation of the $(ZMV)_a$ micron-sized $Yb_2Si_2O_7$ feedstock was used as the crystalline sample and the amorphous sample was obtained by plasma spraying the same powder into distilled cold water. Subsequently, amorphous–crystalline mixtures with weight fractions of 25wt.%–75wt.%, 50wt.%–50wt.%, 75wt.%–25wt.% were prepared and analyzed by XRD as shown in **Figure 2** XRD patterns of 100wt.% crystalline and 100wt.% amorphous samples are also shown in **Figure 2** for comparison. Although a small peak at ~30° of the 100wt. % amorphous powder pattern was observed (see Figure 2, inset graph), the powder was still assumed to be 100% amorphous for the analysis.

2.3.2 Microstructure and porosity

The samples were sectioned, polished, and examined with a scanning electron microscope (Carl Zeiss NTS GmbH, Oberkochen, Germany) combined with an energy-dispersive X-ray INCAEnergy355 spectrometer (EDS, Oxford Instruments Ltd., Abingdon, Oxfordshire, UK). Acquired SEM images were employed to assess the volume fractions of pores in the coatings by means of image analysis using an image thresholding procedure with the analySIS pro software (Olympus Soft Imaging Solutions GmbH,

Germany). The analysis was performed on 10 SEM micrographs (x2000 magnification) per sample, each with a resolution of 1280 x 1100 pixels and covering a horizontal field width of 126 μm.

3. Results and discussion

3.1 Coating deposition

Graphite was used as the substrate material to deposit $Yb_2Si_2O_7$ coatings by different thermal spray techniques. The reason for testing with graphite in the first place was its relatively wide CTE (2-8 × 10^{-6} K^{-1}, [30] mean value range measured from polycrystalline graphite due to its anisotropy) to match with that of $Yb_2Si_2O_7$ (4.1 × 10^{-6} K^{-1} [20]). However, although APS- and VLPPS-deposited coatings remained adherent to graphite during and after deposition, suspension plasma sprayed coating flaked off during the cooling process and no coating could be deposited on graphite by HVOF **Figure 3**. Although it remains unclear, the poor deposition by means of SPS on the graphite might be related to the sub-micron sized feedstock, which contains 39% Yb_2SiO_5 (7.4 × 10^{-6} K^{-1} [17]). As a result, possible higher thermal mismatch stresses arising upon cooling may be responsible for the spallation of the coating. No deposition acquired by HVOF, meanwhile, can be associated with the low mechanical strength of the graphite. It conceivably facilitates the removal of the graphite due to the impact of high-velocity particles and results in a "grit blasting" effect on the substrate instead of deposition. It was possible to obtain successful depositions by SPS and HVOF when the graphite substrates were substituted with carbon steel substrates.

3.2 Amorphous content

The XRD patterns of the as-deposited $Yb_2Si_2O_7$ coatings using different thermal spray methods are shown in **Figure 4**. Several reflection peaks and two broad humps (2θ range of 25-38° and 40-70°) that are observed in the patterns of the APS and SPS coatings clearly reveal an almost fully amorphous phase. Similarly, humps in the 2θ range of 25–38° are also detectable in the patterns of the HVOF and VLPPS

coatings, albeit relatively small and also accompanied with sharp, high-intensity peaks, which suggest the presence of crystalline phases.

$Yb_2Si_2O_7$ shows a type C disilicate structure according to the Felsche classification of RE silicates and its SiO_4 tetrahedra units are known as glass formers [31,32], as they produce highly viscous liquids when they melt. Although a solid crystalline phase is thermodynamically favorable for such liquid when it reaches its melting point, crystallization is kinetically restrained by its high viscosity. If this liquid is rapidly quenched as happens in the plasma spraying process, since the slow mobility of the molecules is further reduced to the point where they cannot move around and create new interfaces for nucleation, it solidifies as a glass. In order to enable crystal growth in this liquid, it would be ideal to allow nucleation above glass transition temperature (T_g) and to maintain this temperature, as crystal growth is a thermally activated process. To that end, aiming crystalline coatings, the practicality of reaching substrate temperatures as high as 1000°C (~ T_g) was investigated in each above-mentioned thermal spray process. To that end, the substrates were heated by spray torches prior to spraying. In APS and SPS, although it was initially possible to reach substrate temperatures of up to 800–900°C (according to pyrometer recordings), the temperature quickly dropped down to 400–600°C until the spraying began and was monitored to be in this range during the deposition. In the controlled atmosphere of the VLPPS chamber, the temperature drop was relatively minor (≈ 50K) and the deposition temperatures during plasma spraying were recorded to be 980°C. Besides, while samples rapidly cooled to room temperature after APS and SPS depositions were completed, it was possible to retain high temperatures of the sample in the VLPPS chamber following deposition. To further reduce the cooling rate, the sample was heated by the plasma flame after the deposition likewise the previous substrate heating. The plasma power used for the heating was gradually reduced within the given time and the sample was steadily cooled to room temperature. As a result of this heat management in the VLPPS process, highly crystallized $Yb_2Si_2O_7$ as-sprayed coatings were obtained, as shown in **Figure 4**, in contrast to APS and SPS methods. A

quantitative comparison of the amorphous contents in each thermally sprayed coating can also be found in **Table 4**.

The crystallization of fully molten particles was found to be strongly reliant on deposition temperatures by comparing the results of plasma spraying processes with each other. While ~98% crystallinity was achieved in the VLPPS process thanks to high deposition temperature as well as the post-deposition plasma heating (effect of it on the crystallinity and microstructure will be further discussed below), very high amorphous contents (~97% in APS, ~87% in SPS) was obtained at moderate deposition temperatures. On the other hand, although the highest deposition temperature obtained with the HVOF flame was 150°C, PONKCS analysis results suggest ~48% amorphous content in the HVOF coating, which is significantly lower than that of APS and SPS coatings. This higher crystallinity in the HVOF coating can be attributed to partially molten/non-molten particle deposition in this method (microstructure will be shown and discussed in the next section) which possibly preserve the crystalline structure.

3.3 Phase composition

The reflection peaks in the patterns of the coatings (**Figure 4**) can be indexed using the diffraction patterns of monoclinic $Yb_2Si_2O_7$ (*C*2/*m*, JCPDS No 01-082-0734), monoclinic Yb_2SiO_5 (*I*2/*a*, JCPDS No 00-040-0386), monoclinic Yb_2SiO_5 ($P2_1/c$, JCPDS No 00-052-1187), and cubic Yb_2O_3 (*Ia*-3, JCPDS No 01-074-1981). Accordingly, crystalline phases in the highly amorphous APS and SPS coatings were found to be Yb_2O_3 (*Ia*-3) and Yb_2SiO_5 (*I*2/*a*, $P2_1/c$). The Yb_2SiO_5 phase with the monoclinic symmetry of $P2_1/c$ was obtained as an intermediate oxidation product of $Yb_4Si_2O_7N_2$ and introduced as a metastable modification of Yb_2SiO_5 for the first time by Kolitsch et al. [33]. More recently, Heng at al. and Richards et al. reported the formation of the Yb_2SiO_5 $P2_1/c$ phase in magnetron-sputtered Yb heavily doped silicon oxide coatings, and in the plasma sprayed $Yb_2Si_2O_7$ (and Yb_2SiO_5) coatings, respectively [20,34]. In both studies, the metastable Yb_2SiO_5 $P2_1/c$ phase was transformed to Yb_2SiO_5 *I*2/*a* after annealing at 1200°C. Since the Yb_2O_3 phase was not detected in the feedstocks, its presence in the APS and SPS coatings can

be explained by silicon loss during spraying, according to the Yb_2O_3-SiO_2 binary phase diagram [35] (**Figure 5**). Silicon loss from the $Yb_2Si_2O_7$ interoxide compound leads to a shift in the composition towards the Yb-rich region. Depending on the extent of the loss, the Yb-rich composition either crystallizes partially or completely into an equilibrium Yb_2SiO_5 phase or eutectic solidification occurs with an eventual Yb_2O_3 product. Depending on whether the composition falls into a hypereutectic or hypoeutectic region, a proeutectic Yb_2SiO_5 or Yb_2O_3 form until the composition reaches the eutectic composition where the remaining solidification follows the eutectic reaction.

3.4 Microstructure

Figure 6 shows a comparison of the microstructures of $Yb_2Si_2O_7$ coatings deposited using the APS, HVOF, SPS, and VLPPS techniques. Due to the elevated substrate temperature by plasma torch prior to spraying and subsequent high-power spraying conditions, fully molten particle deposition with no intrasplat cracks is observed in the APS deposit. A small number of interlamellar cracks in the deposit also imply the remelting of deposited splats with the arrival of the next splats and the promoted diffusion between them at these high deposition temperatures. Nevertheless, a clear interface crack between the two spray passages of the APS deposit is visible (**Figure 6a**). Furthermore, cracks penetrating vertically into the thickness of the coating are found to be present in the APS deposit with a crack density of 3 cracks/mm. Possibly, the origin of these cracks is CTE mismatch resulting in tensile stress development in the highly amorphous and dense coating during the cooling from high deposition temperature to room temperature.

A vertical crack network coupled with branch cracks were also observed in the SPS-deposited $Yb_2Si_2O_7$ coating on the steel substrate with evenly distributed very small pores (**Figure 6b**). Considering that the steel substrate probably has higher CTE than the coating in this case, vertical cracks found in the SPS coating can be called as segmentation cracks and attributed to stress relaxation in the coating during the deposition process. Segmentation crack formation in the SPS coating is a well-known phenomenon and

typically associated with the high torch power used to evaporate the suspension liquid and short spray distances in this process [38,39].

Figure 6c-d show the cross-section of HVOF and VLPPS $Yb_2Si_2O_7$ coatings with relatively dense and vertical crack-free microstructures. Splat/splat boundaries are difficult to discern in these deposits, indicating good adhesion between the splats over a large contact area. Nevertheless, some fine porosity and microcracks are present, resulting from non-molten or partially molten particles embedded in the HVOF microstructure. Some partially molten particles that bonded well with the melted part are also observed in the VLPPS coating. The porosity of HVOF and VLPPS coatings was determined to be 6.6 ± 0.8 % and 3.6 ± 0.4 %, respectively, by image analysis.

Crack-free microstructures of the HVOF and VLPPS coatings can be related to their deposition conditions, residual stress states, and crystallinity. Relatively higher porosity, hence a better strain tolerance, and lower magnitude of CTE mismatch stresses stemming from colder deposition conditions can be assisting the crack-free microstructure in the HVOF process. In the VLPPS, even though the coating is denser and the deposition temperature is rather high, moderate cooling rates (owing to post-deposition plasma heating with gradually reduced power) can be preventing the crack formation. In order to investigate whether there is a relation between the crack-free microstructures of the HVOF and VLPPS coatings and their higher crystallinity, further experiments were conducted. Higher amorphous content in the HVOF and VLPPS coatings was aimed for this purpose. To that end higher amount of methane (200 slpm) giving the stoichiometric fuel/oxygen ratio to obtain maximum flame temperature was used in the HVOF process and no post-deposition plasma heating was applied in the VLPPS. **Figure 9a-b** show the microstructure of these coatings and their XRD patterns are given in **Figure 9c**. According to PONKCS analysis results, ~45 and ~75% crystallinity was obtained in the HVOF and VLPPS deposited coatings, respectively. Although these are not significant decreases in the crystallinity, the impact of the drop on the microstructure of particularly VLPPS coating is evident from the presence of vertical cracks. Eleven cracks were counted in the VLPPS coating through the two cm sample length, whereas no cracks were

observed in the HVOF coating. These results imply that (i) part of the crystallization in the VLPPS takes place during the post-deposition plasma heating, (ii) the increased crystallinity and/or reduced cooling rate with the plasma heating prevent vertical crack formation in the coating. Considering that the crystallinity is lower in the HVOF coating than the VLPPS coating, yet it reveals no cracks likewise the VLPPS, critically different residual stress states in these coatings (due to CTE mismatch with the substrate, differences in deposition temperatures as mentioned above) seem to be playing the major role in the crack formation, assuming no significant differences in their chemistries. Higher magnification BSE-SEM images of the APS and SPS coatings with EDS elemental maps are given in **Figure 7a-b**. Between the changing material contrasts from white to dark gray, various intermediate gray shades appear in the cross-section of the highly amorphous coatings. EDS maps reveal that Yb-rich regions are white due to the high average atomic number, while different gray shades from light to dark show the gradually increasing Si-containing mixtures. Moreover, a number of randomly oriented and elongated fine crystallites were observed in the amorphous matrix of the APS coating, as shown in **Figure 7c**. However, a reliable identification of the composition of these crystallites was not possible due to their small size.

Figure 8a-b show the high-magnification BSE-SEM images of highly crystalline HVOF and VLPPS coatings. According to the XRD data, two phases (Yb_2SiO_5 and $Yb_2Si_2O_7$) are present in these coatings, although more than two different material contrasts were observed in the images. EDS analyses reveal a compositional difference between the white (Yb-rich) and gray (Yb-poor) regions, but not among the areas with various shades of gray. Furthermore, a number of very fine structures were observed in the VLPPS coating, in which one phase is embedded in the matrix of another phase(s) without any apparent orientation relationships (**Figure 8b**, inset). In particular, such structures were commonly found at the splat boundaries of the VLPPS coating, where the Si-evaporation is likely most pronounced. It is possible that these very fine structures are the product of a eutectic solidification or a hypoeutectic/hypereutectic solidification that could not be determined by SEM.

3.5. Summary and conclusions

$Yb_2Si_2O_7$ coatings were deposited by means of APS, HVOF, SPS, and VLPPS thermal spray methods using a commercial and internally synthesized feedstock. The as-sprayed amorphous contents of the coatings were investigated and compared taking into consideration the deposition conditions (deposition temperature, holding time at high-temperature) and particle melting states (molten or non-molten particle deposition) in different processes.

APS and SPS deposited coatings were found to be highly amorphous and vertically cracked. Moreover, evaporation of the Si-bearing species during deposition was found to be particularly pronounced in these processes, leading to the formation of the Yb_2O_3 phase in the as-sprayed coatings.

Almost fully crystalline (~98%) and highly dense $Yb_2Si_2O_7$ coatings could be deposited in the VLPPS chamber as a result of the high deposition temperature and post-deposition plasma heating. It was also found that the latter is influential in preventing the vertical crack formation in the coating.

The HVOF process was found to yield relatively high crystalline (~50%) coatings in contrast to APS- and SPS-deposited coatings (~5-10%) due to the partially molten or non-molten particle deposition. The porosity content of this coating (~7%) was not as low as plasma sprayed coatings, yet no vertical cracks were observed in the HVOF microstructure. This is probably a result of lower deposition temperature, which also lowers the magnitude of the stresses during cooling, and somewhat more strain tolerant microstructure due to higher porosity content.

It can be concluded that the VLPPS is the preferred method among others as an almost fully crystalline, dense coating microstructure without vertical cracks could be obtained with it. Nevertheless, it was found that the cooling conditions need to be carefully tuned to achieve such results. HVOF technique seems to be also promising but further investigations are required to investigate the bonding of HVOF sprayed particles on brittle silicon bond coat. Future studies will generally focus on adhesion of coatings as well as a better understanding of crack formation mechanisms for developing strategies to achieve the best performance. Furthermore, steam cycling tests are planned for validation of the coating systems.

References

1. E.J. Opila, R.E. Hann, Paralinear Oxidation of CVD SiC in Water Vapor, *J. Am. Ceram. Soc.*, **80**(1), 197-205 (1997)
2. R.C. Robinson, J.L. Smialek, SiC Recession Caused by SiO_2 Scale Volatility under Combustion Conditions: I, Experimental Results and Empirical Model, *J. Am. Ceram. Soc.*, **82**(7), 1817-1825 (1999)
3. E.J. Opila, J.L. Smialek, R.C. Robinson, D.S. Fox, N.S. Jacobson, SiC Recession Caused by SiO_2 Scale Volatility under Combustion Conditions: II, Thermodynamics and Gaseous-Diffusion Model, *J. Am. Ceram. Soc.*, **82**(7), 1826-1834 (1999)
4. J.L. Smialek, R.C. Robinson, E.J. Opila, D.S. Fox, N.S. Jacobson, SiC and Si_3N_4 recession due to SiO_2 scale volatility under combustor conditions, *Adv. Compos. Mater*, **8**(1), 33-45 (1999)
5. N.P. Bansal, Handbook of ceramic composites ed. by Narottam P. Bansal. [E-Book], Kluwer, 2005
6. N.S. Jacobson, Corrosion of Silicon-Based Ceramics in Combustion Environments, *J. Am. Ceram. Soc.*, **76**(1), 3-28 (1993)
7. K.N. Lee, Current status of environmental barrier coatings for Si-Based ceramics, *Surf. Coat. Technol.*, **133–134**, 1-7 (2000)
8. H.E. Eaton, G.D. Linsey, K.L. More, J.B. Kimmel, J.R. Price, N. Miriyala, EBC Protection of SiC/SiC Composites in the Gas Turbine Combustion Environment, ASME Turbo Expo 2000: Power for Land, Sea, and Air, 2000, American Society of Mechanical Engineers, p V004T002A018
9. H.E. Eaton, G.D. Linsey, E.Y. Sun, K.L. More, J.B. Kimmel, J.R. Price, N. Miriyala, EBC Protection of SiC/SiC Composites in the Gas Turbine Combustion Environment: Continuing Evaluation and Refurbishment Considerations, ASME Turbo Expo 2001: Power for Land, Sea, and Air, 2001, American Society of Mechanical Engineers, p V004T002A010
10. K.N. Lee, D.S. Fox, J.I. Eldridge, D. Zhu, R.C. Robinson, N.P. Bansal, R.A. Miller, Upper Temperature Limit of Environmental Barrier Coatings Based on Mullite and BSAS, *J. Am. Ceram. Soc.*, **86**(8), 1299-1306 (2003)
11. K.N. Lee, D.S. Fox, N.P. Bansal, Rare earth silicate environmental barrier coatings for SiC/SiC composites and Si_3N_4 ceramics, *J. Eur. Ceram. Soc.*, **25**(10), 1705-1715 (2005)
12. K.N. Lee, R.A. Miller, N.S. Jacobson, New Generation of Plasma-Sprayed Mullite Coatings on Silicon Carbide, *J. Am. Ceram. Soc.*, **78**(3), 705-710 (1995)
13. C.M. Weyant, K.T. Faber, Processing–microstructure relationships for plasma-sprayed yttrium aluminum garnet, *Surf. Coat. Technol.*, **202**(24), 6081-6089 (2008)
14. C. Friedrich, R. Gadow, T. Schirmer, Lanthanum hexaaluminate—a new material for atmospheric plasma spraying of advanced thermal barrier coatings, *J. Therm. Spray Technol.*, **10**(4), 592-598 (2001)
15. G. Pracht, R. Vaßen, D. Stöver, Lanthanum-Lithium Hexaaluminate—A New Material for Thermal Barrier Coatings in Magnetoplumbite Structure—Material and Process Development, Advanced Ceramic Coatings and Interfaces: Ceramic Engineering and Science Proceedingsed., John Wiley & Sons, Inc., 2008, p 87-99
16. K.N. Lee, R.A. Miller, N.S. Jacobson, Plasma sprayed mullite coatings on silicon-base ceramics, ed., Google Patents, 1995
17. B.T. Richards, H.N.G. Wadley, Plasma spray deposition of tri-layer environmental barrier coatings, *J. Eur. Ceram. Soc.*, **34**(12), 3069-3083 (2014)
18. F. Stolzenburg, P. Kenesei, J. Almer, K.N. Lee, M.T. Johnson, K.T. Faber, The influence of calcium–magnesium–aluminosilicate deposits on internal stresses in $Yb_2Si_2O_7$ multilayer environmental barrier coatings, *Acta Mater.*, **105**, 189-198 (2016)

19. H. Zhao, B.T. Richards, C.G. Levi, H.N.G. Wadley, Molten silicate reactions with plasma sprayed ytterbium silicate coatings, *Surf. Coat. Technol.*, **288**, 151-162 (2016)
20. B.T. Richards, H. Zhao, H.N.G. Wadley, Structure, composition, and defect control during plasma spray deposition of ytterbium silicate coatings, *Journal of Materials Science*, **50**(24), 7939-7957 (2015)
21. B.T. Richards, S. Sehr, F. de Franqueville, M.R. Begley, H.N.G. Wadley, Fracture mechanisms of ytterbium monosilicate environmental barrier coatings during cyclic thermal exposure, *Acta Mater.*, **103**, 448-460 (2016)
22. G. Mauer, M.O. Jarligo, D.E. Mack, R. Vaßen, Plasma-Sprayed Thermal Barrier Coatings: New Materials, Processing Issues, and Solutions, *J. Therm. Spray Technol.*, **22**(5), 646-658 (2013)
23. X.Q. Cao, R. Vassen, W. Jungen, S. Schwartz, F. Tietz, D. Stöver, Thermal Stability of Lanthanum Zirconate Plasma-Sprayed Coating, *J. Am. Ceram. Soc.*, **84**(9), 2086-2090 (2001)
24. M.O. Jarligo, D.E. Mack, R. Vassen, D. Stöver, Application of Plasma-Sprayed Complex Perovskites as Thermal Barrier Coatings, *J. Therm. Spray Technol.*, **18**(2), 187-193 (2009)
25. M.O. Jarligo, G. Mauer, D. Sebold, D.E. Mack, R. Vaßen, D. Stöver, Decomposition of $Ba(Mg_{1/3}Ta_{2/3})O_3$ perovskite during atmospheric plasma spraying, *Surf. Coat. Technol.*, **206**(8–9), 2515-2520 (2012)
26. K. Korpiola, J.P. Hirvonen, L. Laas, F. Rossi, The influence of nozzle design on HVOF exit gas velocity and coating microstructure, *J. Therm. Spray Technol.*, **6**(4), 469-474 (1997)
27. N. Schlegel, S. Ebert, G. Mauer, R. Vaßen, Columnar-Structured Mg-Al-Spinel Thermal Barrier Coatings (TBCs) by Suspension Plasma Spraying (SPS), *J. Therm. Spray Technol.*, **24**(1), 144-151 (2015)
28. A. Vardelle, C. Moreau, J. Akedo, H. Ashrafizadeh, C.C. Berndt, J.O. Berghaus, M. Boulos, J. Brogan, A.C. Bourtsalas, A. Dolatabadi, M. Dorfman, T.J. Eden, P. Fauchais, G. Fisher, F. Gaertner, M. Gindrat, R. Henne, M. Hyland, E. Irissou, E.H. Jordan, K.A. Khor, A. Killinger, Y.-C. Lau, C.-J. Li, L. Li, J. Longtin, N. Markocsan, P.J. Masset, J. Matejicek, G. Mauer, A. McDonald, J. Mostaghimi, S. Sampath, G. Schiller, K. Shinoda, M.F. Smith, A.A. Syed, N.J. Themelis, F.-L. Toma, J.P. Trelles, R. Vassen, P. Vuoristo, The 2016 Thermal Spray Roadmap, *J. Therm. Spray Technol.*, **25**(8), 1376-1440 (2016)
29. N.V.Y. Scarlett, I.C. Madsen, Quantification of phases with partial or no known crystal structures, *Powder Diffr.*, **21**(4), 278-284 (2006)
30. J.B. Nelson, D.P. Riley, The thermal expansion of graphite from 15°c. to 800°c.: part I. Experimental, *Proceedings of the Physical Society*, **57**(6), 477 (1945)
31. J. Felsche, The crystal chemistry of the rare-earth silicates, Rare Earthsed., Springer Berlin Heidelberg, 1973, p 99-197
32. D. Hülsenberg, A. Harnisch, A. Bismarck, Microstructuring of Glasses, Springer Berlin Heidelberg, 2008
33. U. Kolitsch, V. Ijevskii, H.J. Seifert, I. Wiedmann, F. Aldinger, Formation and general characterization of a previously unknown ytterbium silicate (A-type Yb2SiO5), *Journal of Materials Science*, **32**(23), 6135-6139 (1997)
34. C.L. Heng, J.T. Li, W.Y. Su, Z. Han, P.G. Yin, T.G. Finstad, The formation of Yb silicates and its luminescence in Yb heavily doped silicon oxides after high temperature annealing, *Opt. Mater.*, **42**, 17-23 (2015)
35. N.A. Toropov, I.A. Bondar', Silicates of the rare earth elements, *Bulletin of the Academy of Sciences of the USSR, Division of chemical science*, **10**(8), 1278-1285 (1961)
36. K. Ito, H. Kuriki, H. Araki, S. Kuroda, M. Enoki, Detection of segmentation cracks in top coat of thermal barrier coatings during plasma spraying by non-contact acoustic emission method, *Science and Technology of Advanced Materials*, **15**(3), 035007 (2014)
37. H.B. Guo, R. Vaßen, D. Stöver, Atmospheric plasma sprayed thick thermal barrier coatings with high segmentation crack density, *Surf. Coat. Technol.*, **186**(3), 353-363 (2004)

38. R. Vaßen, H. Kaßner, G. Mauer, D. Stöver, Suspension Plasma Spraying: Process Characteristics and Applications, *J. Therm. Spray Technol.*, **19**(1), 219-225 (2010)
39. D. Waldbillig, O. Kesler, Effect of suspension plasma spraying process parameters on YSZ coating microstructure and permeability, *Surf. Coat. Technol.*, **205**(23–24), 5483-5492 (2011)
40. A. Killinger, R. Gadow, G. Mauer, A. Guignard, R. Vaßen, D. Stöver, Review of New Developments in Suspension and Solution Precursor Thermal Spray Processes, *J. Therm. Spray Technol.*, **20**(4), 677-695 (2011)
41. M. Marr, O. Kesler, Permeability and Microstructure of Suspension Plasma-Sprayed YSZ Electrolytes for SOFCs on Various Substrates, *J. Therm. Spray Technol.*, **21**(6), 1334-1346 (2012)
42. B.T. Richards, K.A. Young, F. de Francqueville, S. Sehr, M.R. Begley, H.N.G. Wadley, Response of ytterbium disilicate–silicon environmental barrier coatings to thermal cycling in water vapor, *Acta Mater.*, **106**, 1-14 (2016)
43. S. Ueno, T. Ohji, H.-T. Lin, Recession behavior of a silicon nitride with multi-layered environmental barrier coating system, *Ceram. Int.*, **33**(5), 859-862 (2007)
44. S. Ramasamy, S.N. Tewari, K.N. Lee, R.T. Bhatt, D.S. Fox, Slurry based multilayer environmental barrier coatings for silicon carbide and silicon nitride ceramics — I. Processing, *Surf. Coat. Technol.*, **205**(2), 258-265 (2010)
45. M.P. Appleby, D. Zhu, G.N. Morscher, Mechanical properties and real-time damage evaluations of environmental barrier coated SiC/SiC CMCs subjected to tensile loading under thermal gradients, *Surf. Coat. Technol.*, **284**, 318-326 (2015)
46. P. Mechnich, Y_2SiO_5 coatings fabricated by RF magnetron sputtering, *Surf. Coat. Technol.*, **237**, 88-94 (2013)
47. D.D. Jayaseelan, S. Ueno, T. Ohji, S. Kanzaki, Sol–gel synthesis and coating of nanocrystalline $Lu_2Si_2O_7$ on Si_3N_4 substrate, *Mater. Chem. Phys.*, **84**(1), 192-195 (2004)

Tables

Table 1: EBC systems manufactured by means of different processing techniques. MS and DS in the material compositions stand for mono- and disilicate, respectively.

EBC system and materials	**Process**	**Ref.**
Si/Mullite/YbMS or YbDS Si/YbDS	Plasma spray into a box furnace	[11] [17] [18] [19] [42]
LuDS/LuDS-Mullite/**LuDS**	Plasma spray	[43]
Mullite/GdMS	Slurry-based dip-coat processing	[44]
HfO_2-Si/(Yb,Gd)DS	Electron beam- physical vapor deposition (EB-PVD)	[45]
YMS	RF magnetron sputtering	[46]
LuDS	Sol–gel	[47]

Table 2: Particle size of the $Yb_2Si_2O_7$ feedstock used for each individual thermal spray process.

	Particle size (µm)		
Thermal spray process	d_{10}	d_{50}	d_{90}
APS	24	38	68
HVOF	22	33	48
VLPPS	35	49	68
SPS	0.5	0.7	1.06

Table 3: Thermal spraying conditions for $Yb_2Si_2O_7$: APS, HVOF, VLPPS, and SPS. The number of passes or deposition time for each set of parameters was adjusted to obtain 150–200µm coating thickness.

APS	
Parameters	**Settings**
Plasma gas composition (slpm)	46Ar/4H_2
Current (A)	520
Power (kW)	57
Stand-off distance (mm)	90
Robot speed (mm/s)	500
Feed rate (%)	30
Carrier gas (%)	2.5
Number of passes	2
Cooling	none
Substrate temperature (°C)	400
Deposition temperature (°C)	575

HVOF

Parameters	**Settings**
Oxygen flow (slpm)	395
Methane flow (slpm)	190
Air flow (slpm)	250
Feed rate (%)	20
Stand-off distance (mm)	325
Robot velocity (mm/s)	1200
Number of passes	5
Cooling	none
Deposition temperature (°C)	125–150

VLPPS

Parameters	**Settings**
Plasma gas composition (slpm)	110Ar/20He
Chamber pressure (Pa)	200
Feed rate (%)	25
Current (A)	2100
Stand-off distance (mm)	700
Power (kW)	90
Robot velocity (mm/s)	15
Deposition temperature (^{0}C)	980
Deposition duration (min)	2

SPS

Parameters	**Settings**
Plasma gas comp. (slpm)	184Ar/37H_2/24.5N_2
Current (A)	250
Stand-off distance (mm)	70
Feed rate (g/min)	30
Robot velocity (mm/s)	500
Number of passes	18
Deposition temperature (^{0}C)	500
Cooling	0.3 MPa press. air

Table 4: Phase composition and amorphous content of the as-sprayed coatings determined by the PONKCS method. Deposition temperatures recorded for each process are also given for a comparison.

	APS	SPS	HVOF	VLPPS
$Yb_2Si_2O_7$ (wt. %)			49.0	93.0
Yb_2SiO_5 (I2/a) (wt. %)	0.5	2.0	3.0	5.0
Yb_2SiO_5 (P21/c) (wt. %)		2.5		
Yb_2O_3 (wt. %)	2.5	8.5		
Amorphous (wt.%)	97.0	87.0	48.0	2.0
Deposition Temperature (°C)	575	500	125-150	980

Figure captions

Figure 1: XRD pattern of (a) micron and (b) submicron sized $Yb_2Si_2O_7$ powder (insets show the back-scattered SEM images of corresponding powders).

Figure 2: XRD patterns of 100wt.% A (A=amorphous), 75wt.%A–25wt.%C (C=crystalline), 50wt.%A–50wt.%C, 25wt.%A–75wt.%C, and 100wt.% C powder and powder mixtures.

Figure 3: First trials of $Yb_2Si_2O_7$ depositions by (a) SPS and (b) HVOF processes on graphite substrates.

Figure 4: XRD patterns of as-sprayed $Yb_2Si_2O_7$ coatings deposited by means of different thermal spray techniques.

Figure 5: Yb_2O_3-SiO_2 pseudo-binary phase diagram (redrawn from [31]).

Figure 6: Backscattered SEM (BSE-SEM) micrographs of as-sprayed $Yb_2Si_2O_7$ coatings by (a) APS, (b) SPS, (c) HVOF, and (d) VLPPS thermal spray methods. Black arrows indicate the vertical cracks, green arrows indicate the interpassage crack, white arrows indicate branch cracks, blue arrows indicate the partially or non-molten particles and gray arrows indicate the pores in the images.

Figure 7: High-magnification BSE-SEM micrographs of as-sprayed $Yb_2Si_2O_7$ coatings by (a) APS, and (b) (SPS). Red and blue boxes indicate the recorded elemental mapping region of the images by EDS (a1-a3, b1-b3). Elongated crystal growth observed in the (c) APS-deposited $Yb_2Si_2O_7$ coating.

Figure 8: High-magnification BSE-SEM micrographs of as-sprayed $Yb_2Si_2O_7$ coatings by (a) HVOF, (b) VLPPS, and corresponding EDS spectra (a1 and b1). Inset in (b) displays a higher magnification image of a splat boundary.

Figure 9: SEM micrographs of (a) an HVOF coating deposited with stoichiometric methane/oxygen ratio (200/395) and (b) a VLPPS coating deposited without post-deposition plasma heating. The XRD patterns of these two coatings are given in (c).

Figure 1

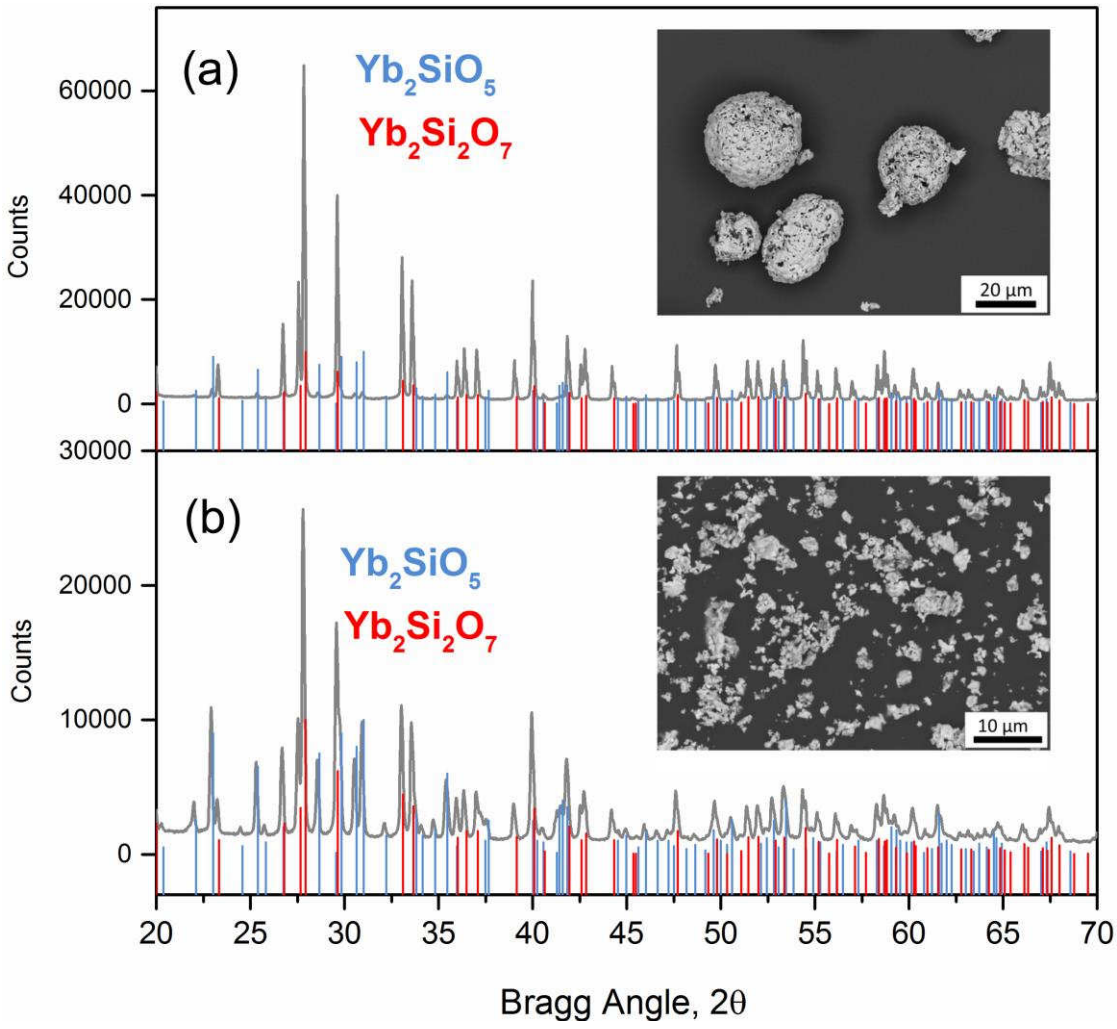

Figure 2

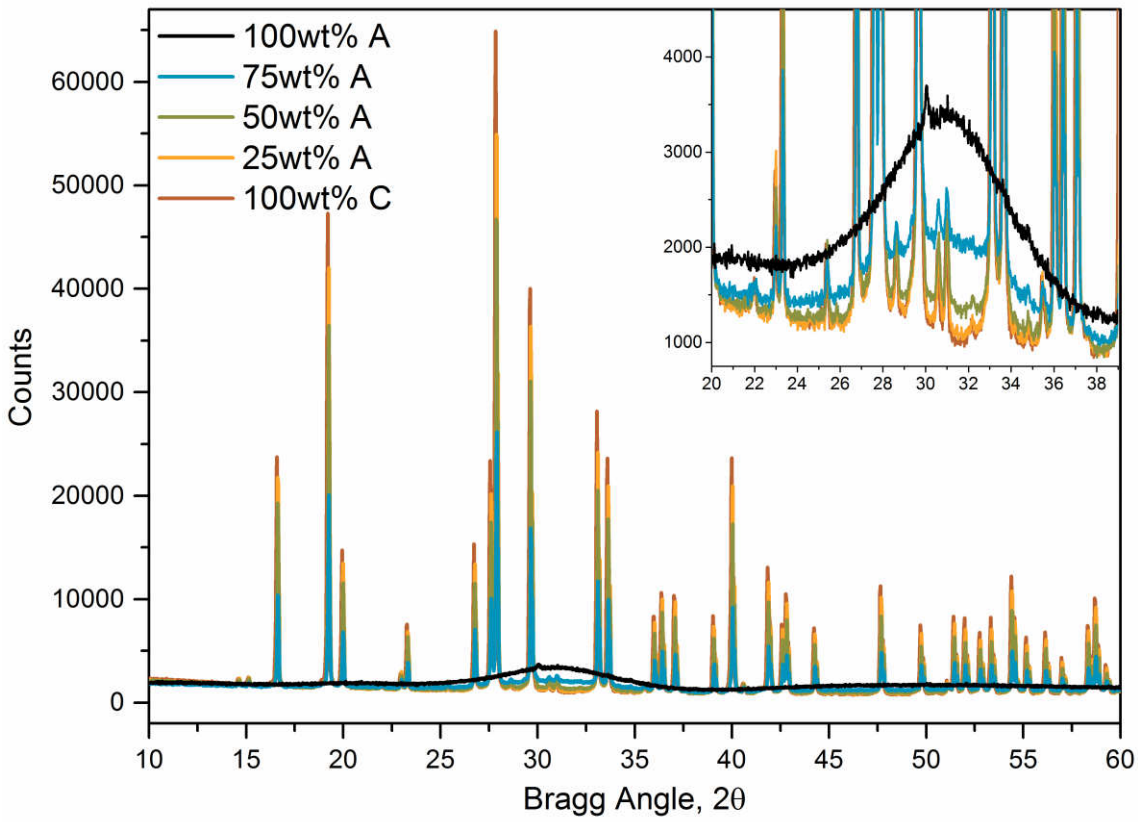

Figure 3

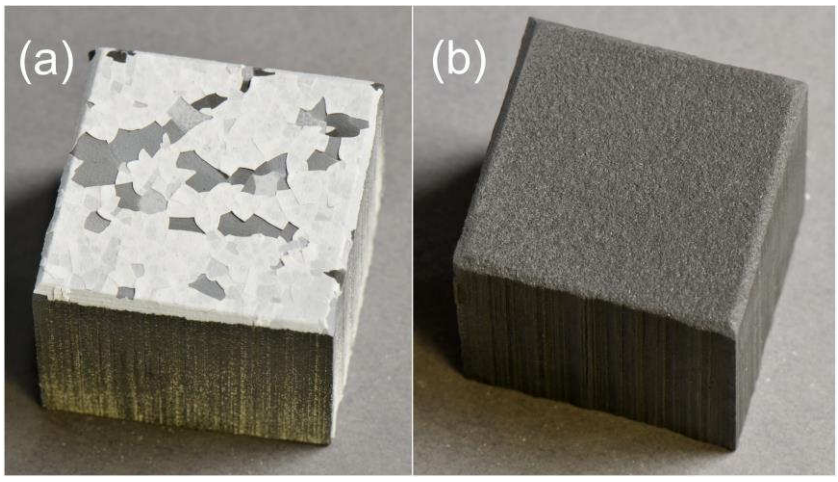

Figure 4

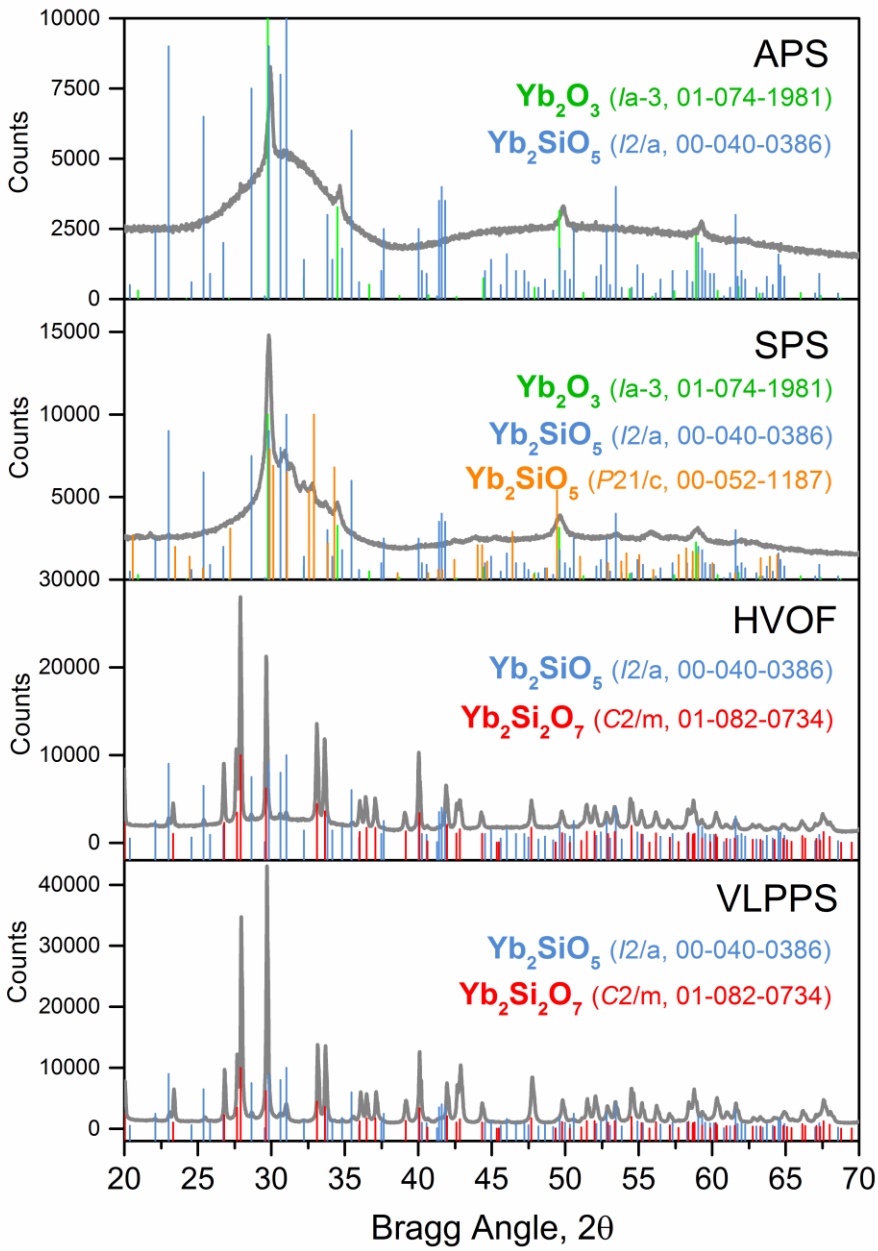
APS
Yb2O3 (Ia-3, 01-074-1981)
Yb2SiO5 (I2/a, 00-040-0386)
SPS
Yb2O3 (Ia-3, 01-074-1981)
Yb2SiO5 (I2/a, 00-040-0386)
Yb2SiO5 (P21/c, 00-052-1187)
HVOF
Yb2SiO5 (I2/a, 00-040-0386)
Yb2Si2O7 (C2/m, 01-082-0734)
VLPPS
Yb2SiO5 (I2/a, 00-040-0386)
Yb2Si2O7 (C2/m, 01-082-0734)
Counts
Bragg Angle, 2θ

Figure 5

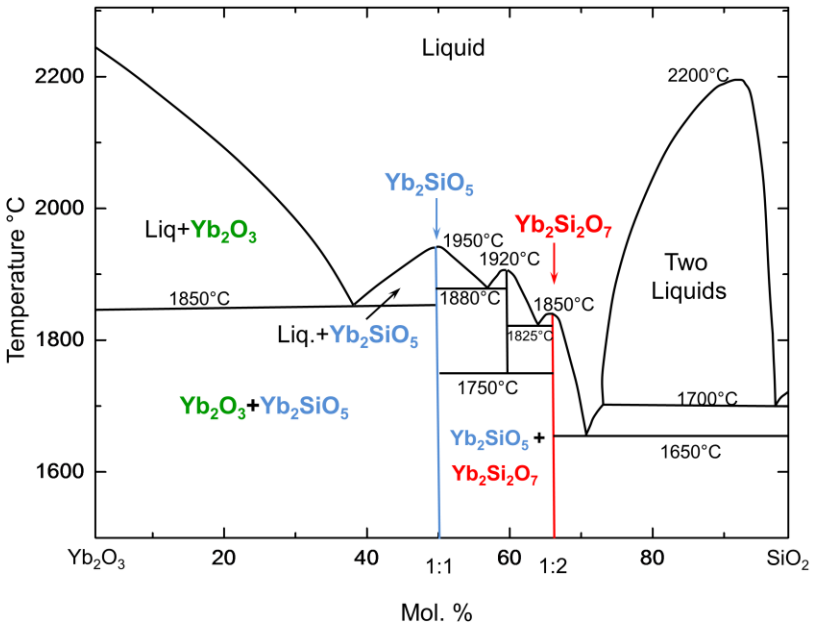
Liquid
2200
2000
1800
1600
Temperature °C
2200°C
Yb2SiO5
Yb2Si2O7
Liq+Yb2O3
1950°C
1920°C
Two
Liquids
1850°C
1880°C
1850°C
1825°C
Liq.+Yb2SiO5
1750°C
1700°C
Yb2O3+Yb2SiO5
Yb2SiO5 +
Yb2Si2O7
1650°C
Yb2O3
20
40
1:1
60
1:2
80
SiO2
Mol. %

Figure 6

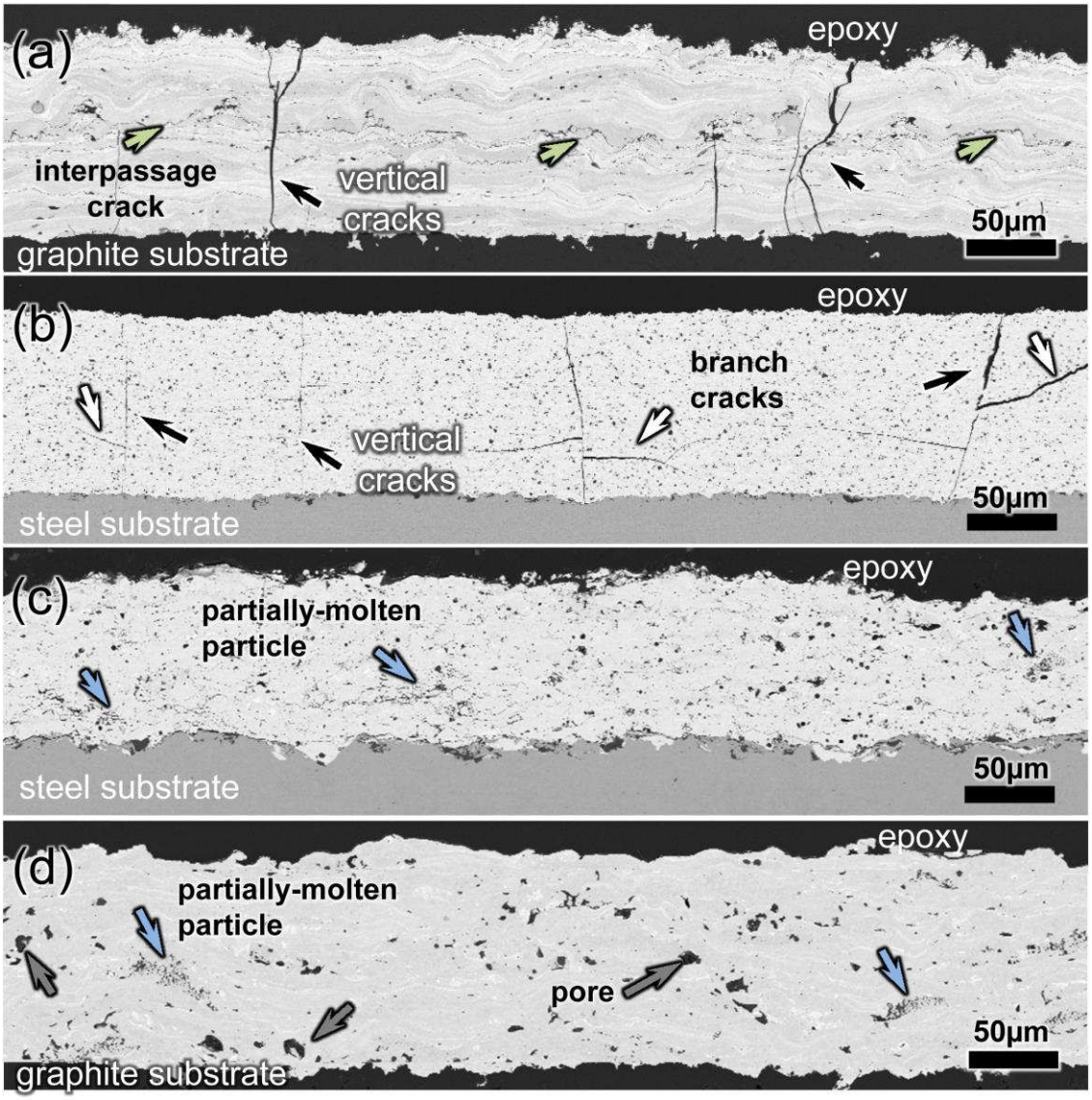
(a)
epoxy
interpassage crack
vertical cracks
graphite substrate
50μm
(b)
epoxy
branch cracks
vertical cracks
steel substrate
50μm
(c)
epoxy
partially-molten particle
steel substrate
50μm
(d)
epoxy
partially-molten particle
pore
graphite substrate
50μm

Figure 7

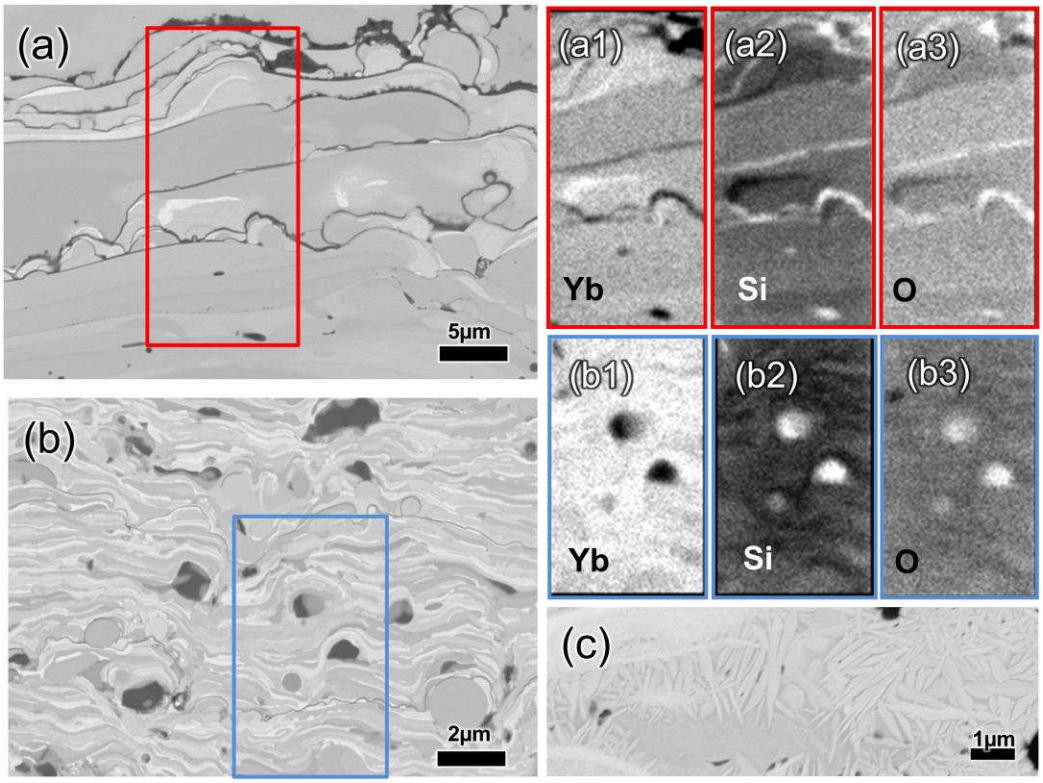

Figure 8a

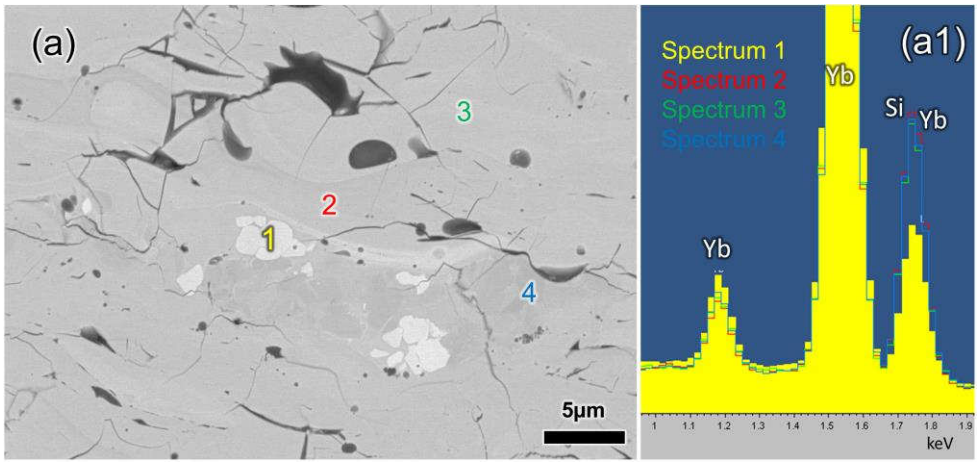

Figure 8b

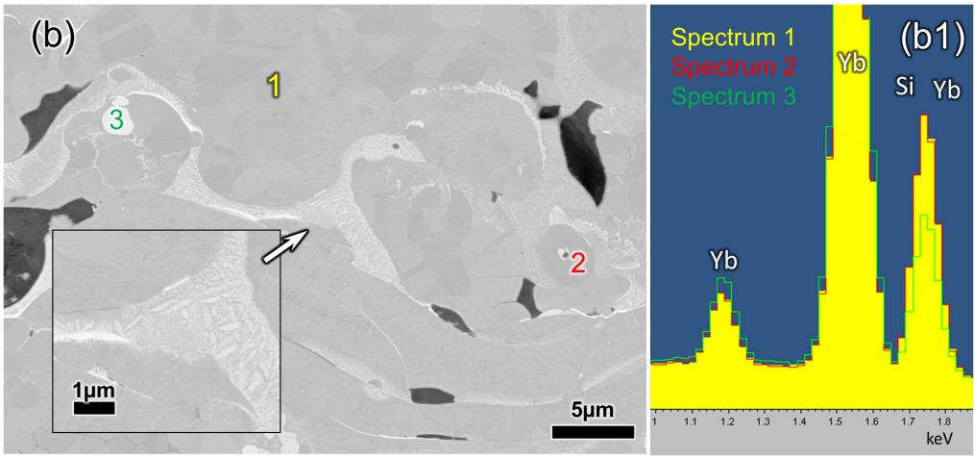

Figure 9a

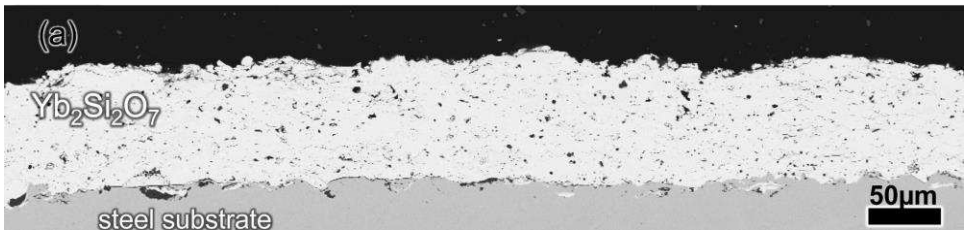

Figure 9b

Figure 9c

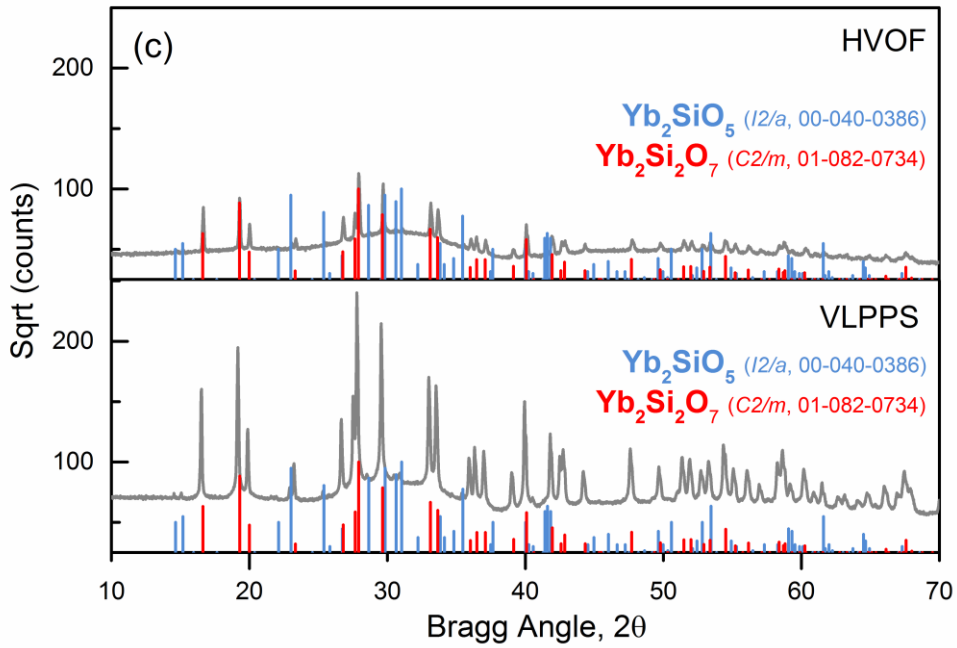
(c)
HVOF
Yb2SiO5 (I2/a, 00-040-0386)
Yb2Si2O7 (C2/m, 01-082-0734)
VLPPS
Yb2SiO5 (I2/a, 00-040-0386)
Yb2Si2O7 (C2/m, 01-082-0734)
Sqrt (counts)
200
100
200
100
10
20
30
40
50
60
70
Bragg Angle, 2θ